Virtual Moment of Inertia-Based Independent Dual-Speed Regulation of Brushless Dual Rotor Machines

Hui Wu[1], Shuangxia Niu[1], *Senior Member*, *IEEE*, Zekai Lyu[1], Mingyuan Jiang[1], Chunhua Liu[2], *Senior Member*, *IEEE*, Wei Liu[1], *Senior Member*, *IEEE*, K.T. Chau[1], *Fellow*, *IEEE*

***Abstract*— Brushless dual rotor machines (BLDRMs) are emerging as a promising solution for applications requiring multiple energy flows due to their dual electric ports and dual mechanical ports. For counter-rotating propellers in underwater and aerial vehicles, achieving independent dual-speed control is essential. However, the dual-inertia characteristic of BLDRMs makes it difficult to directly apply speed controller tuning methods developed for the single-inertia machines. Besides, the inherent coupling between speed and torque in dual rotors can further degrade control performance. In this paper, the concept of virtual moment of inertia (VMI) is first proposed based on the electromechanical models, enabling the BLDRMs to be equivalently transformed into conventional single-inertia machines. Building on VMI, a model compensation-based active disturbance rejection control (MC-ADRC) strategy is proposed to further decouple and achieve independent speed regulation. Specifically, state equations are derived based on the outer rotor speed and the speed difference between the dual rotors, treating torque coupling as a lumped disturbance. Comprehensive details regarding the controller design and parameter selection criteria are provided to ensure the practical implementation of various types of BLDRM structures and certain other multi-port machines. Finally, experiments are conducted on a BLDRM drive platform to validate the effectiveness of the proposed method.**

***Index Terms*— Active disturbance rejection control, brushless dual rotor machines, dual-electrical-port dual-mechanical-port machines, dual speed control, magnetic gear machine, virtual moment of inertia**

I. INTRODUCTION

A traditional electric machine typically consists of a single set of windings and only one rotor. In applications involving multiple energy flows like hybrid electric vehicles (HEVs) [1], coordination of multiple motors is often necessary, assisted by power split tools such as planetary gears; however, this approach results in a larger system size and increased structural complexity. In recent years, to enhance system integration and compactness, research on electrical continuously variable transmission (E-CVT) for HEVs [2]-[4] has led to the development of dual rotor machines (DRM) characterized by dual-electric port and dual-mechanical port configurations. DRMs feature two sets of windings and two rotors, allowing operation in multiple modes and facilitating the transfer of mechanical and electrical energy between multiple ports [5][6]. Among these, brushless DRMs (BLDRMs) are gaining prominence compared to the brush DRMs due to their enhanced reliability, attributed to the absence of brushes and slip rings [7]-[10].

BLDRMs are typically designed based on the principle of magnetic field modulation [7]. These motors can be viewed as two parts [10], i.e., dual rotors and modulation winding form a magnetic gear machine (MGM) [11], while a rotor and regular winding constitute a standard permanent magnet synchronous machine (PMSM). The unique structure of BLDRMs allows for flexible selection of operating and control modes tailored to different application scenarios. Potential applications include E-CVTs, wind power generation, counter-rotating propeller drives for underwater and aerial vehicles [12]-[20].

For BLDRMs used in E-CVTs for HEVs, one rotor is typically connected to an internal combustion engine (ICE), while the other rotor is linked to the vehicle's wheels. The modulation winding operates in torque control mode to maintain the ICE working at optimal efficiency [12]-[14]. Depending on whether the MGM and PMSM are in generator or motor mode, energy can flow in multiple directions to satisfy the torque demands across various vehicle operating conditions [15][16]. In wind power generation, BLDRM typically operates in two scenarios. First, both rotors are connected to wind blades, with both MGM and PMSM operating in generator mode. Torque control mode can be applied to enable dual maximum power point tracking [17]. Second, one rotor is connected to a blade while the other is free-spinning. The modulation winding is set to speed control mode, ensuring the free-spinning rotor maintains a constant speed, achieving variable speed constant frequency output suitable for direct grid supply [18][19].

For counter-rotating propeller drives, rotors are connected to counter-rotating propellers [20], with the MGM and PMSM operating in motor mode. Both sets of windings should be in speed control mode to achieve independent speed control of the dual rotors. According to [21], the system operates more efficiently when the two propellers run at different speeds, necessitating variable speed control for both rotors. However, research on this application scenario is limited. The primary control challenge lies in coupling speed and torque within the BLDRMs. Specifically, the electromagnetic torque generated by the MGM affects both the operation of the outer and inner rotors, and the positions of the dual rotors are jointly fed back to the controller for coordinate transformation, which in turn influences the generated torque, while the PMSM part just

This work is supported by the Research Grant Council, Hong Kong, China, under Collaborative Research Fund C1052-21GF. (*Corresponding author: Shuangxia Niu*)

Hui Wu, Shuangxia Niu, Zekai Lyu, Mingyuan Jiang, Wei Liu, and K.T. Chau are with the Department of Electrical and Electronic Engineering, The Hong Kong Polytechnic University, Hong Kong, SAR, China (e-mail: hui12138.wu@connect.polyu.hk; eesxniu@polyu.edu.hk; zekai.lyu@polyu.edu.hk; m.y.jiang@polyu.edu.hk; wei.liu@polyu.edu.hk; k.t.chau@polyu.edu.hk).

Chunhua Liu is with the School of Energy and Environment, City University of Hong Kong, Hong Kong, SAR, China (e-mail: chunliu@cityu.edu.hk).

affects the outer rotor. In other words, the MGM part and the PMSM part are coupled. Traditional proportional-integral (PI) controllers have poor decoupling performance and limited bandwidth [22]. Besides, the mechanical model of the BLDRMs differs significantly from that of conventional PMSMs due to the multiple ports and the coupled torque and speed, making it difficult to directly apply PI speed controller tuning methods developed for PMSMs to BLDRMs, thus complicating parameter selection and increasing the time required for trial-and-error adjustments.

To address torque coupling in BLDRM, a PI controller with feedforward compensation was employed in [23], but precise model parameters are required, limiting effectiveness and leaving unknown disturbances unaddressed. The deadbeat-direct torque and flux control (DTFC) proposed by [22] achieves torque and flux linkage decoupling with fast response but involves a complex design. Notably, these methods are not applied in dual-speed control scenarios. Instead, one rotor is consistently driven by either an ICE or a servo motor. Besides, the principles for selecting controller parameters are not clearly specified.

In addition, numerous advanced robust control strategies and torque-decoupling techniques have been successfully applied to PMSMs, including sliding mode control (SMC), model predictive control (MPC), and disturbance observers (DOB), among others., As a nonlinear control technique, SMC offers strong robustness against both internal and external disturbances [24]-[26], and is widely used in systems with parameter variations or uncertainties. However, its inherent chattering effect can lead to steady-state oscillations in rotor position. Given that the modulation unit in BLDRM typically has a high number of pole pairs, this chattering may be further amplified, resulting in a more severe torque ripple produced by the modulation winding. Finite control set MPC also provides advantages such as strong robustness, elimination of the need for pulse width modulation, and fast dynamic response. Nevertheless, its steady-state performance is relatively poor, and multi-step prediction requires substantial computational resources [27]-[29]. DOB estimates disturbances by comparing the actual system output with the nominal model output, thereby enabling torque decoupling [24][30]. However, the effectiveness of observers relies on accurate model parameters. For BLDRM, which is a multivariable system with partially complex and difficult-to-calculate dynamics, constructing an accurate model is evidently challenging.

Compared to these methods, active disturbance rejection control (ADRC), first proposed in [31], has attracted significant attention due to its inherent decoupling capability and parameter robustness. ADRC treats deviations from the nominal model as lumped disturbances and employs an extended state observer (ESO) for their estimation and compensation [32], [33]. Typically, only one control parameter is related to the model, which greatly simplifies parameter tuning. Its strong robustness also makes ADRC particularly suitable for BLDRM systems with pronounced coupling characteristics.

This article addresses the dual-speed control of BLDRM. First, the structure and comprehensive electrical and mechanical models of the BLDRM are presented. Then, the concept of virtual moment of inertia (VMI) is proposed and systematically derived. Leveraging this, a model compensation-based active disturbance rejection control (MC-ADRC) strategy is proposed in the dual speed loop of the BLDRM drive system, where the outer rotor speed and the speed difference between the dual rotors are utilized as state variables, respectively. The main contributions of this article are as follows:

1) The notion of VMI is proposed and derived based on the electromechanical characteristics of the BLDRM. The coupled dual-inertia BLDRM can be equivalently transformed into two conventional single-inertia machines, which provides theoretical support for tuning the speed controller.

2) Based on the VMI, an MC-ADRC strategy is developed, further enhancing the disturbance rejection capability and improving parameter robustness. Independent dual-speed regulation for BLDMR is achieved.

3) Comprehensive details regarding the controller design are provided, along with the criteria for selecting control parameters. This ensures the practical implementation of various types of BLDRM structures. Meanwhile, the proposed method also provides valuable guidance for dual speed control in certain other multi-port machines.

The rest of this article is organized as follows. In Section II, the structure of a BLDRM is given. In Section III, the mathematical model is introduced. In Section IV, the VMI is proposed, and the design process of the VMI-based MC-ADRC strategy is presented. Moreover, the disturbance rejection performance and robustness are analyzed. Experimental results are presented in Section V. Finally, Section VI concludes this article.

II. Structure of BLDRM

The structure of the BLDRM for analysis and subsequent control is proposed by [13] and illustrated in Fig. 1(a). This structure features two rotors and two sets of windings. The stator houses both the modulation winding and the regular winding, with the regular winding located on the inner side of the stator and the modulation winding on the outer side. Besides, the inner rotor is composed of iron teeth, offering simplicity and robustness.

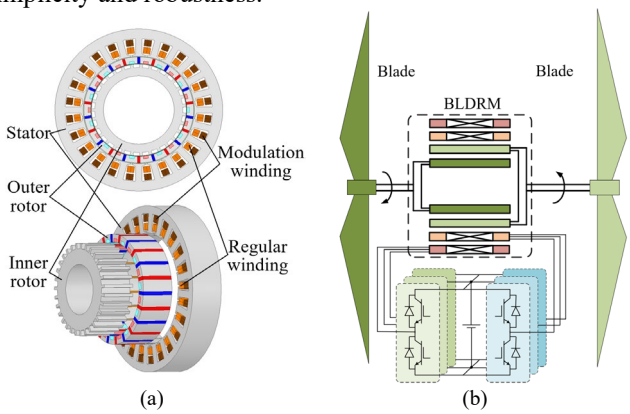

Fig. 1. (a) The structure of BLDRM [13]. (b) Counter-rotating propellers using BLDRM.

For applications involving counter-rotating propellers in underwater and aerial vehicles, the overall framework is

depicted in Fig. 1(b). The inner and outer rotors are connected to blades with opposing force surfaces. Power is supplied to the two sets of windings via inverters, driving the dual rotors to rotate in opposite directions. This setup propels the fluid to generate a force in a consistent direction. The counter-rotation of the blades results in the cancellation of the torques generated, thereby preventing yaw and facilitating easier heading control. This is the primary advantage of counter-rotating propellers [20].

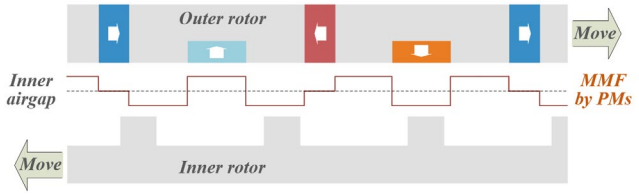

Fig. 2. Illustration of the MMF generated by PMs in the inner airgap.

Unlike conventional BLDRMs, this machine structure incorporates spoke-type permanent magnets (PMs) on the outer rotor and additionally inserts radially magnetized PMs on the inner side of the outer rotor to enhance the third harmonic in the inner airgap. The magnetomotive force (MMF) in the inner airgap is depicted in Fig. 2. This design strategically utilizes the third-order harmonic for magnetic field modulation by coordinating the pole pair numbers, thereby enhancing the electromagnetic torque exerted by the modulation winding on dual rotors. Compared to other conventional BLDRMs, this approach further increases torque density, although it also intensifies the torque coupling between the two rotors, making this BLDRM a more challenging control subject.

As previously mentioned, the regular winding and the outer rotor form a conventional PMSM through the outer airgap, with the regular winding and the spoke-type PMs on the outer rotor sharing the same pole pair number of 11. Meanwhile, the modulation winding and the dual rotors form an MGM through the inner airgap, where the outer rotor acts as the magnetic field modulation module using the third harmonic. According to the magnetic field modulation principle [8], to generate a constant electromagnetic torque, the pole pair numbers of the modulation winding, p_{mw}, outer rotor, p_{ro}, and inner rotor, p_{ri}, must satisfy (1).

$$p_{mw} = 3p_{ro} - p_{ri} \tag{1}$$

Specifically, p_{mw} is designed as 2, p_{ro} is set to 11, and p_{ri} is designed as 31, which means that the inner rotor is composed of 31 iron teeth.

III. Mathematical Model of BLDRM

In this section, the mechanical equations of the MGM will first be introduced. Then, the comprehensive electrical and mechanical models of the BLDRM are presented.

According to the magnetic field modulation principles [8], for the MGM part, the relationship of electromagnetic torques satisfies (2).

$$T_{em} : T_{rom} : T_{ri} = p_{mw} : 3p_{ro} : p_{ri} \tag{2}$$

where T_{em} respects the electromagnetic torques produced by the modulation winding, T_{rom} and T_{ri} are the electromagnetic torques acting on the outer and inner rotors, respectively.

It is noteworthy that, for clarity, torque is represented in scalar form. According to the principle of magnetic field modulation, the torques produced by the modulation winding on the inner and outer rotors are in opposite directions. Specifically, T_{em} and T_{ri} act in the same direction, while T_{em} is opposite to T_{rom}. Meanwhile, the positive directions of the dual rotors' speed are defined as opposite in the analysis to represent the counter-rotating operation. Thus, the electrical angular velocities satisfy (3).

$$\omega_m = \omega_o + \omega_i \tag{3}$$

where ω_m represents the corresponding electrical angular velocity of the modulation winding's current frequency, ω_o and ω_i are the electrical angular velocities of the outer and inner rotors, respectively.

To derive the mathematical model of the BLDRM, it is assumed that the airgap magnetic field is sinusoidal and that magnetic saturation is not considered. Additionally, based on the calculated self and mutual inductances shown in Fig. 3, where the subscript "*m*" denotes the modulation winding and "*r*" refers to the regular winding, the mutual inductances between the two sets of windings are significantly smaller compared to their respective self and mutual inductances. Therefore, the mutual inductance between the two sets of windings can be considered negligible.

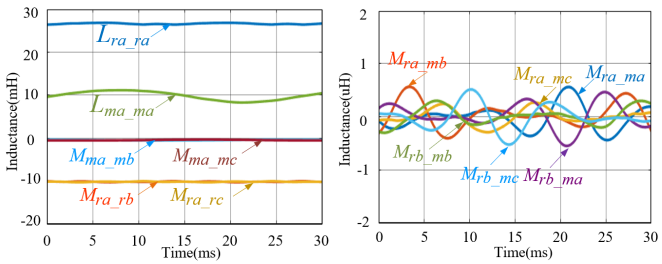

Fig. 3. Calculated inductance. (a) Self and mutual inductances of windings. (b) Mutual inductances between windings.

Applying the coordinate transformation, the equivalent electrical model of the BLDRM is shown in Fig. 4.

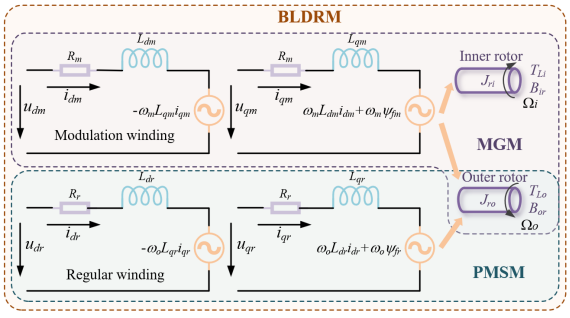

Fig. 4. Equivalent electrical model of BLDRM.

From the equivalent electrical model, it is evident that although the two windings are decoupled, torque and speed coupling exists between the MGM and PMSM. Specifically, the outer rotor is driven by two electromagnetic torques, and

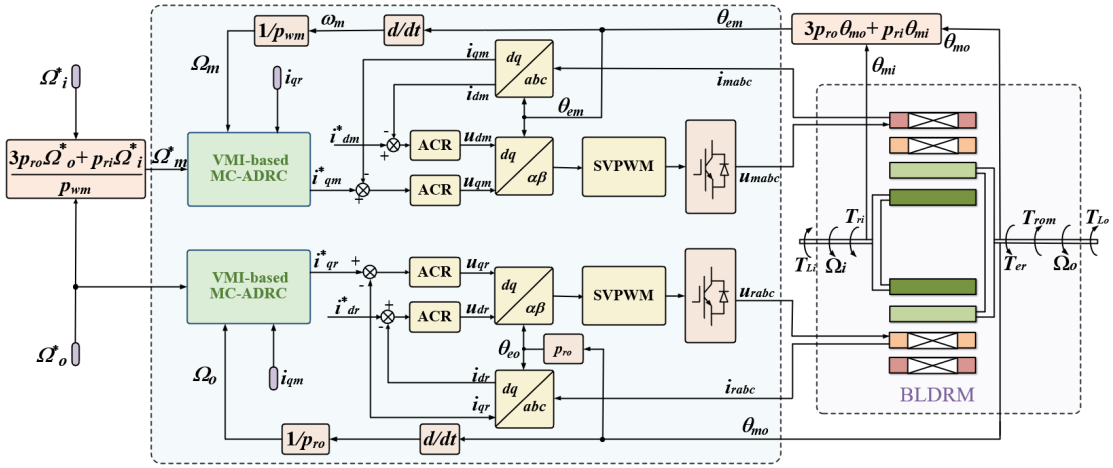

Fig. 6. Schematic of the dual speed control for the BLDRM drive system.

the motion of both rotors simultaneously influences the modulation winding. Therefore, it is necessary to transform this dual-inertia BLDRM into two equivalent single-inertia systems.

The flux linkage equation of the BLDRM is shown as (4):

$$\begin{bmatrix}\psi_{dm}\\ \psi_{qm}\\ \psi_{dr}\\ \psi_{qr}\end{bmatrix}=\begin{bmatrix}L_{dm}i_{dm}\\ L_{qm}i_{qm}\\ L_{dr}i_{dr}\\ L_{qr}i_{qr}\end{bmatrix}+\begin{bmatrix}\psi_{fm}\\ 0\\ \psi_{fr}\\ 0\end{bmatrix} \tag{4}$$

where $\psi_{d/q}$ represent the flux linkages of d/q axis, and $L_{d/q}$ are the inductances of d/q axis. ψ_{fr} is the flux linkage generated by the spoke-type PMs of the outer rotor, and ψ_{fm} is the modulated flux linkage generated by the radial-magnetized PMs of the outer rotor and the inner rotor teeth.

The voltage equation of the BLDRM is deduced as (5):

$$\begin{bmatrix}u_{dm}\\ u_{qm}\\ u_{dr}\\ u_{qr}\end{bmatrix}=\begin{bmatrix}R_m i_{dm}\\ R_m i_{qm}\\ R_r i_{dr}\\ R_r i_{qr}\end{bmatrix}+\frac{d}{dt}\begin{bmatrix}L_{dm}i_{dm}\\ L_{qm}i_{qm}\\ L_{dr}i_{dr}\\ L_{qr}i_{qr}\end{bmatrix}+\begin{bmatrix}-\omega_m L_{qm}i_{qm}\\ \omega_m L_{dm}i_{dm}\\ -\omega_o L_{qr}i_{qr}\\ \omega_o L_{dr}i_{dr}\end{bmatrix}+\begin{bmatrix}0\\ \omega_m\psi_{fm}\\ 0\\ \omega_o\psi_{fr}\end{bmatrix} \tag{5}$$

where $u_{d/q}$ are the voltages of the d/q axis. R represents resistance. $i_{d/q}$ are the currents of the d/q axis. d/dt is the differential operator.

The electromagnetic torque equation of the BLDRM is shown as (6):

$$\begin{bmatrix}T_{em}\\ T_{er}\end{bmatrix}=\frac{3}{2}\begin{bmatrix}-p_{mw}\psi_{qm} & p_{mw}\psi_{dm} & 0 & 0\\ 0 & 0 & -p_{ro}\psi_{qr} & p_{ro}\psi_{dr}\end{bmatrix}\begin{bmatrix}i_{dm}\\ i_{qm}\\ i_{dr}\\ i_{qr}\end{bmatrix} \tag{6}$$

where T_{em} and T_{er} represent the electromagnetic torques produced by modulation and regular winding, respectively.

The mechanical equations for dual rotors are derived as (7):

$$\begin{cases}\dot{\Omega}_o=\dfrac{1}{J_{ro}}(T_{er}+T_{rom}-T_{Lo}-B_{or}\Omega_o+D_o)\\ \dot{\Omega}_i=\dfrac{1}{J_{ri}}(T_{ri}-T_{Li}-B_{ir}\Omega_i+D_i)\end{cases} \tag{7}$$

where "o" means outer rotor, while "i" means inner rotor, Ω_o and Ω_i are the mechanical angular velocities of outer and inner rotors, respectively. $J_{ro/ri}$ are the moments of inertia of dual rotors, respectively. $T_{Lo/Li}$ are the load torque acting on the dual rotors. $B_{or/ir}$ are the viscosity coefficients of the dual rotors, respectively.

Notably, $D_{o/i}$ represent the unmodeled components in the equations, primarily including the coupling torque generated between the inner and outer rotors due to the mutual attraction between the PMs and the iron cores, as shown in Fig. 2, the cogging torque between the outer rotor and the stator, etc.

The calculated coupling torque at counter-rotating 100 rpm for dual rotors is illustrated in Fig. 5 when the windings are not energized. It can be seen that, compared to the theoretical output torques of the dual rotors of the BLDRM, which are designed as 25.22 N·m and 23.69 N·m, respectively [13], the coupling torque is relatively small, accounting for approximately 2% and 1% of the respective values. Therefore, under rated load conditions, the coupling torque can be neglected, but under light load conditions, these coupling torques need to be considered. As a novel machine, the precise modeling and analysis of cogging torque and inter-rotor forces in BLDRM are still at an early stage, and relevant research literature remains limited. Since it is challenging to establish a definitive physical expression for this torque, it is categorized as an unmodeled item in this study. In subsequent control processes, it is treated as a disturbance, which is estimated and compensated for by the observer.

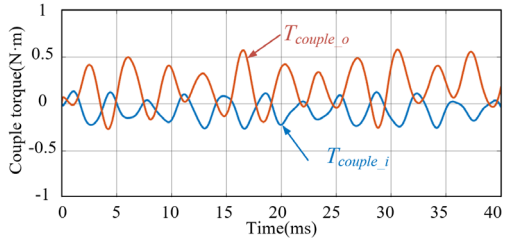

Fig. 5. Calculated coupling torque.

IV. Proposed Independent Dual-Speed Regulation Method of BLDRM

The proposed BLDRM drive system, as shown in Fig. 6, utilizes the dual closed-loop structure based on field-oriented control (FOC) for both sets of windings. The speed of the outer rotor is controlled by the regular winding, while the speed difference between the dual rotors is managed by the modulation winding, thereby indirectly controlling the speed of the inner rotor. The VMI-based MC-ADRC is employed in the dual speed loops. Due to the negligible mutual inductance between the two sets of windings, conventional PI control is employed as the automatic current regulator (ACR) in the current loops. In addition, the i_d reference value is set to zero to optimize torque output and simplify control design. The voltage commands are then processed through Park and Clarke transformations and input into the space vector pulse width modulation (SVPWM) module, generating discrete switching signals fed into two three-phase inverters. Notably, the input electrical angle corresponds to the difference in electrical angles between the dual rotors in the Park transformation for the modulation winding.

In this section, the VMI is first derived based on the electromechanical equations provided by the BLDRM. Then, the detailed design process of the VMI-based MC-ADRC controller is presented, followed by a comprehensive analysis of the controller's performance.

A. Derivation of VMI

According to (7), the electromagnetic torque generated by the regular winding, T_{er}, only affects the speed of the outer rotor. Therefore, if the coupling torque and the torque produced by the modulation winding are both considered external load torque, the system can be equivalently treated as controlling the speed of a conventional PMSM. This equivalence enables a straightforward controller design, where the control target is the speed of the outer rotor, and the controller output is the reference value for the q-axis current of the regular winding.

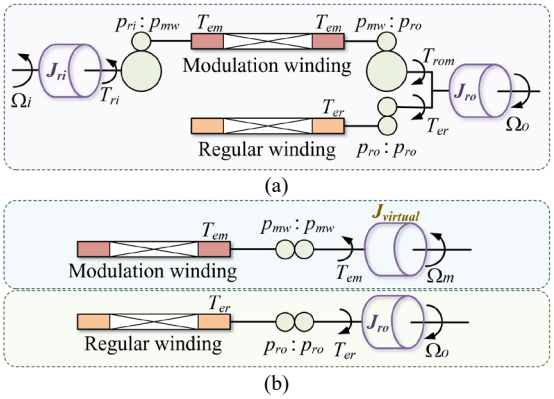

Fig. 7. Mechanical representation of BLDRM. (a) Actual coupled dual-inertia model. (b) Equivalent model of two conventional single-inertia machines.

In contrast, the torque produced by the modulation winding, T_{em}, affects both dual rotors, shown in Fig. 7(a). The control target of the speed regulator is the corresponding mechanical angular velocity of the modulation winding, defined as Ω_m, and the controller output is the reference value for the q-axis current of the modulation winding. Therefore, it is necessary to derive the relationship between Ω_m and T_{em}, which will be used to design the controller.

According to (3), the relationship of mechanical angular velocities can be deduced as:

$$\Omega_m = \frac{3p_{ro}\Omega_o + p_{ri}\Omega_i}{p_{mw}} \tag{8}$$

Differentiating (8) and substituting (2) and (7), it can be deduced that:

$$\begin{aligned}\dot{\Omega}_m = &\underbrace{\left[\left(\frac{3p_{ro}}{p_{mw}}\right)^2\frac{1}{J_{ro}}+\left(\frac{p_{ri}}{p_{mw}}\right)^2\frac{1}{J_{ri}}\right]T_{em}}_{\text{control section}} + \underbrace{\frac{3p_{ro}}{p_{mw}J_{ro}}T_{er}}_{\text{known disturbance}} \\ &\underbrace{+\frac{3p_{ro}}{p_{mw}J_{ro}}\left(-T_{Lo}-B_{or}\Omega_o+D_o\right)-\frac{p_{ri}}{p_{mw}J_{ri}}\left(-T_{Li}-B_{ir}\Omega_i+D_i\right)}_{\text{unknown disturbance}}\end{aligned} \tag{9}$$

where the rate of change of Ω_m is influenced by three components: the first is the control section, determined by T_{em}; the second is the known disturbance, based on T_{er}, which can be calculated by the model parameter and the current of regular winding; and the last is the unknown disturbance, which includes external load torques, frictional torque, and the coupling torque between the dual rotors.

According to (9), the relationship between Ω_m and T_{em} can be equivalently expressed as the mechanical equation for a conventional single-inertia machine, allowing the definition of a virtual moment of inertia $J_{virtual}$. The equivalent inertia model is shown in Fig. 7(b). It can be seen that by introducing VMI, the originally coupled dual-inertia BLDRM is equivalently transformed into two decoupled conventional single-inertia machines, where T_{em} controls Ω_m while T_{er} controls Ω_o. Therefore, parameter tuning algorithms developed for single-inertia machines can be employed. The value of $J_{virtual}$ depends on the actual moments of inertia of the dual rotors as well as the pole pair numbers of both the dual rotors and the modulation winding, given by:

$$J_{virtual} = \frac{p_{mw}^2 J_{ro} J_{ri}}{(3p_{ro})^2 J_{ri} + p_{ri}^2 J_{ro}} \tag{10}$$

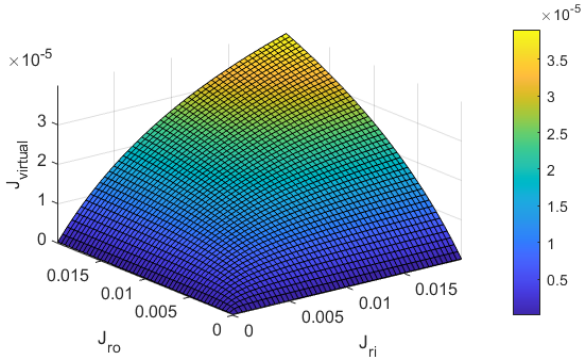

Fig. 8. 3D plot of $J_{virtual}$ as a function of J_{ri} and J_{ro}.

The pole pair numbers are determined during the manufacturing process and remain constant. However, J_{ri} and J_{ro} may change under different loads. This inaccuracy in estimating J_{ri} and J_{ro} affects the accuracy of $J_{virtual}$, which in turn influences the controller parameters and may lead to

suboptimal results. In the machine studied in this paper, a 3D plot of $J_{virtual}$ as a function of J_{ri} and J_{ro} is shown in Fig. 8.

As shown, the value of $J_{virtual}$ is much smaller than that of J_{ri} and J_{ro} (typically one percent to one thousandth of their values). However, the overall trend of $J_{virtual}$ is consistent with that of J_{ri} and J_{ro}; when J_{ri} and J_{ro} simultaneously fluctuate by ±50%, the variation range of $J_{virtual}$ is also ±50%.

With the introduction of VMI, established PI speed controller tuning techniques for PMSMs become applicable to BLDRMs, thereby greatly simplifying the tuning process and reducing the time spent on trial-and-error adjustments.

Similarly, for BLDRMs based on the magnetic field modulation, the harmonic orders for the modulation and the configuration of pole pairs (including their additive or subtractive relationships) directly affect the torque directions and speed ratios for the dual rotors and the modulating winding. Consequently, the VMI formula must be adapted accordingly. The general form can be expressed as:

$$J_{virtual} = \frac{p_{mw}^2 J_{ro} J_{ri}}{(ip_{ro})^2 J_{ri} \pm (jp_{ri})^2 J_{ro}} \tag{11}$$

where i and j denote the harmonic orders involved in modulation. Typically, the fundamental harmonic ($i = j = 1$) dominates in the air gap. However, as in this work, higher-order harmonics are intentionally enhanced and selected for modulation to further increase torque density (i.e., $i = 3, j = 1$). By adjusting the expression according to the modulated magnetic field design and the corresponding pole pair numbers of each machine, the concept can be generalized to other magnetic field modulation-based BLDRM and facilitates potential extension to other multi-port machines.

B. Design of VMI-based MC-ADRC for BLDRM

As shown in (7) and (9), multiple forms of torque disturbances influence the speeds of dual rotors. To further achieve decoupling between the dual rotors, enhance the disturbance rejection capability of the drive system, and improve robustness to model parameters, the MC-ADRC strategy, building on VMI, is proposed for the BLDRM. To this end, the state-space equations must first be established, where Ω_o and Ω_m are selected as state variables, and the modulation and regular winding currents are designated as control inputs.

Substituting (6) into (9), the speed state equations can be deduced as (12):

$$\begin{cases} \dot{\Omega}_{m/o} = b_{m/r} i_{qm/r} + f_{0m/r} + f_{m/r} \\ f_{0m} = \dfrac{9p_{ro}^2}{2J_{ro}p_{mw}} \psi_{fr} i_{qr} \qquad f_{0r} = \dfrac{9}{2J_{ro}} p_{ro} \psi_{fm} i_{qm} \\ f_m = \dfrac{3p_{ro}}{J_{ro}p_{mw}}(-T_{Lo} - B_{or}\Omega_o + D_o) - \dfrac{p_{ri}}{J_{ri}p_{mw}}(-T_{Li} - B_{ir}\Omega_i + D_i) \\ f_r = \dfrac{1}{J_{ro}}(-T_{Lo} - B_{or}\Omega_o + D_o) \end{cases} \tag{12}$$

where f_{0m} and f_{0r} are calculable known disturbances, while f_m and f_r represent difficult-to-calculate unknown disturbances, which need to be estimated by the ESO, and $b_{m/r}$ represents the actual model parameters, which will be utilized in the controller, given as:

$$\begin{cases} b_m = \dfrac{3p_{mw}\psi_{fm}}{2J_{virtual}} \\ b_r = \dfrac{3p_{ro}\psi_{fr}}{2J_{ro}} \end{cases} \tag{13}$$

It is clear that b_m is calculated from the VMI, the pole pairs number, and the corresponding flux linkage. b_r is calculated from the pole pairs number, the moment of inertia of the outer rotor, and the corresponding flux linkage.

The block diagram of VMI-based MC-ADRC is illustrated in Fig. 9. The state variables and the corresponding lumped disturbances are estimated by the ESOs. The disturbances are then fed back and compensated for in the outputs of the controller, thereby mitigating the impact of actual disturbances.

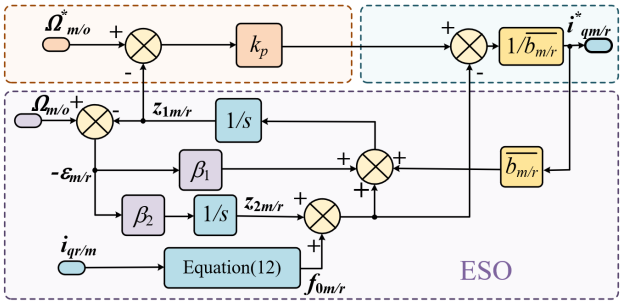

Fig. 9. The block diagram of MC-ADRC.

The expressions of ESOs are shown in (14):

$$\begin{cases} \varepsilon_{1m/r} = z_{1m/r} - \Omega_{m/o} \\ \dot{z}_{1m/r} = z_{2m/r} - \beta_1 \varepsilon_{1m/r} + f_{0m/r} + \bar{b}_{m/r} i^*_{qm/r} \\ \dot{z}_{2m/r} = -\beta_2 \varepsilon_{1m/r} \end{cases} \tag{14}$$

where $z_{1m/r}$ are the estimations of the state variables, i.e., $\Omega_{m/o}$, $\varepsilon_{1m/r}$ are the estimation errors, $z_{2m/r}$ are the estimations of the unknown disturbances, and $\beta_{1/2}$ are the gain coefficients of the ESO. $i^*_{qm/r}$ represent the output of the controller, i.e., q-axis current reference. To reduce the number of parameters and facilitate tuning, the same set of gain coefficients is chosen for both ESOs. $\bar{b}_{m/r}$ are the model parameters used in the controller, which should closely align with the actual model parameters, i.e., $b_{m/r}$. The robustness of the parameters will be discussed afterwards.

According to the estimations of ESO, the q-axis current references for modulation and regular windings can be calculated as follows:

$$i^*_{qm/r} = \frac{k_p(\Omega^*_{m/o} - z_{1m/r}) - (f_{0m/r} + z_{2m/r})}{\bar{b}_{m/r}} \tag{15}$$

where k_p denotes the control gain coefficient.

Regarding the criteria for determining the controller parameters, the VMI-based MC-ADRC controller is tuned using the bandwidth method [32]. In the dual-speed control of the BLDRM, since both speed loops utilize the same

bandwidth value based on the inverter's switching frequency, the parameters for both controllers are set identically. The k_p aligns with the speed loop's bandwidth. The ESO gain coefficients are configured as $[\beta_1, \beta_2]^T = [2\omega_{eso}, \omega_{eso}^2]^T$, where the observer bandwidth ω_{eso} is generally three to five times k_p.

C. Performance Analysis

a) Disturbance Rejection Performance

In the VMI-based MC-ADRC controller, ESO is expected to estimate the disturbance accurately and quickly, which is critical for the control performance. Thus, the disturbance estimation capability of ESO is analyzed first.

According to (14), in the frequency domain, the disturbance estimation error transfer function G_e from disturbance $f_{m/r}$ to the estimation error $f_{m/r}$-$z_{2m/r}$ is deduced as:

$$G_e(s) = \frac{f_{m/r}(s) - z_{2m/r}(s)}{f_{m/r}(s)} = \frac{s^2 + \beta_1 s}{s^2 + \beta_1 s + \beta_2} = \frac{s^2 + 2\omega_{eso} s}{(s + \omega_{eso})^2} \quad (16)$$

The disturbance rejection transfer function G_f from disturbance $f_{m/r}$ to the speed $\Omega_{m/o}$ can be deduced as:

$$G_f(s) = \frac{\Omega_{m/o}(s)}{f_{m/r}(s)} = \frac{s^2 + (k_p + \beta_1)s}{s^3 + (k_p + \beta_1)s^2 + (k_p\beta_1 + \beta_2)s + k_p\beta_2} \quad (17)$$

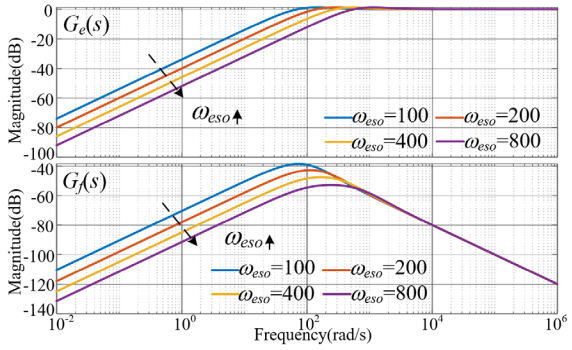

Fig. 10. Magnitude plot of G_e and G_f with different ω_{eso}.

The Bode plots of G_e and G_f are displayed in Fig. 10. As ω_{eso} increases, the magnitude curve of G_e shifts downward, indicating that the observer's bandwidth for disturbance observation increases, thereby enhancing its estimation capability. Similarly, the magnitude curve of G_f also shifts downward, suggesting that the influence of disturbances on the speed is further mitigated, and the controller's ability to suppress disturbances is improved.

b) Robustness Analysis

As mentioned, in the proposed controller, only $\bar{b}_{m/r}$ is related to the motor, including the pole pair numbers of the modulation winding and dual rotors, the motor inertias of the dual rotors, and the flux linkages. The inertias may be inaccurately measured, and the flux linkages may dynamically change during motor operation, leading to parameter deviations. To analyze the effect of parameter mismatches on disturbance rejection performance, speed reference tracking performance, and the noise suppression performance, the transfer function G_f from disturbance $f_{m/r}$ to speed $\Omega_{m/o}$, $G_t(s)$ from the speed reference to speed, and $G_n(s)$ from the noise to speed can be deduced as follows:

$$\begin{cases} G_f(s) = \dfrac{\Omega_{m/o}(s)}{f_{m/r}(s)} = \dfrac{s^2 + (k_p + \beta_1)s}{s^3 + (k_p + \beta_1)s^2 + \dfrac{b_{m/r}}{\bar{b}_{m/r}}\left[(k_p\beta_1 + \beta_2)s + k_p\beta_2\right]} \\ G_t(s) = \dfrac{\Omega_{m/o}(s)}{\Omega^*_{m/o}(s)} = \dfrac{k_p(s^2 + \beta_1 s + \beta_2)}{\dfrac{\bar{b}_{m/r}}{b_{m/r}}(s^2 + k_p s + \beta_1 s)s + (k_p\beta_1 + \beta_2)s + k_p\beta_2} \\ G_n(s) = \dfrac{\Omega_{m/o}(s)}{N_{m/o}(s)} = \dfrac{(k_p\beta_1 + \beta_2)s + k_p\beta_2}{\dfrac{\bar{b}_{m/r}}{b_{m/r}}(s^2 + k_p s + \beta_1 s)s + (k_p\beta_1 + \beta_2)s + k_p\beta_2} \end{cases} \quad (18)$$

The Bode plots of G_f, G_t, and G_n with $\bar{b}_{m/r}$ ranging from 0.1 to 5 times its nominal value, $b_{m/r}$, are shown in Fig. 11. As illustrated, when $\bar{b}_{m/r}$ = 0.1*$b_{m/r}$ (i.e., the estimated inertia is higher than the actual value), the overall magnitude of G_f decreases, indicating enhanced disturbance rejection ability and decreased speed fluctuations during sudden load changes. However, the magnitude may increase within a certain frequency band, resulting in weakened harmonic suppression capability at that frequency. The magnitude of G_t exceeds 0 dB in the mid-frequency range, indicating speed overshoot during step reference tracking, which affects dynamic performance and leads to suboptimal results. Additionally, the magnitude of G_n increases in the high-frequency range, suggesting a reduction in the overall ability to suppress high-frequency noise, which may cause increased speed fluctuations during steady-state operation.

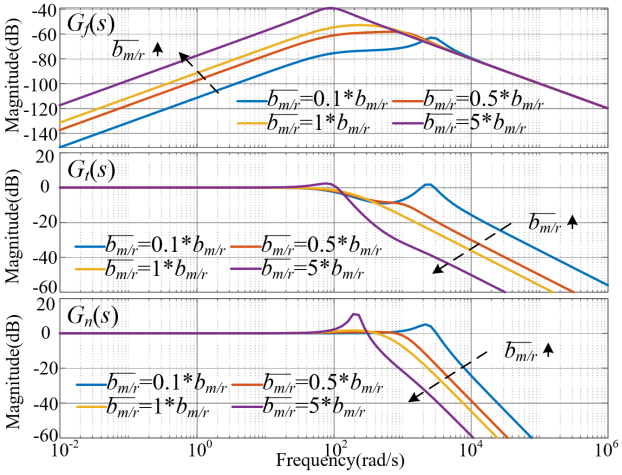

Fig. 11. Magnitude plot of G_f, G_t, and G_n under model parameter mismatch (k_p = 157, ω_{eso} = 628).

When $\bar{b}_{m/r}$ = 5*$b_{m/r}$ (i.e., the estimated inertia is lower than the actual value), the overall magnitude of G_f increases, indicating reduced disturbance rejection and greater sensitivity to disturbances, resulting in increased speed fluctuations during sudden load changes. The magnitude of G_t exceeds 0 dB in certain frequency bands, similarly affecting dynamic performance. The overall magnitude of G_n decreases, indicating improved suppression of high-frequency noise; however, the magnitude increases within a

specific frequency band, leading to weakened noise suppression capability at that frequency.

Overall, through the performance analyses described above, the validity of the proposed controller is fully illuminated.

V. Experimental Validation

To verify the effectiveness of the proposed control strategy, the experiment is conducted on the BLDRM drive system using the dSPACE MicroLabBox DS1202 platform, as shown in Fig. 12. As can be seen, the dual rotors are both connected to the magnetic powder brakes, which provide the load torque when the rotors are running. Both modulation winding and regular winding are driven by three-phase two-level voltage source inverters. The DC voltage is set to 200 V. The sampling and control frequencies are set to 10 kHz, i.e., the switching period, T_s, is 100 us. The PI controller parameters in the current loop are tuned to $K_{Pm/r} = L_{m/r}/(3T_s)$, $K_{Im/r} = R_{m/r}/(3T_s)$, where the values of $R_{m/r}$ and $L_{m/r}$ are obtained through measurements using a Wheatstone bridge. The detailed parameters of the tested BLDRM are given in Table I.

The bandwidth of the speed control loop is set to 25 Hz, 1/400 of the switching frequency of the inverter. Because the machine is designed for low speed and high torque [13], the speed reference is 100 rpm, and the load torque is about 10 N·m. For fairness, the VMI-based PI speed controller is also tuned according to the bandwidth of the speed loop [34]. The parameters are calculated as: $K_{Pm} = 0.023$, $K_{Im} = 0.07$, $K_{Pr} = 8.5$, $K_{Ir} = 20$. For MC-ADRC, $k_p = 157$ rad/s, $\omega_{eso} = 628$ rad/s, Besides, $\overline{b}_{r/m}$ are 87 and 6580 Wb/(kg·m^2) respectively, calculated from the parameters of the BLDRM model as (13). Notably, the defined positive directions for the inner and outer rotors are opposite.

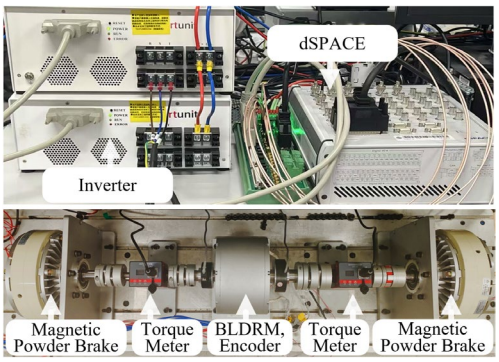

Fig. 12. Experimental platform of BLDRM drive system.

TABLE I
Main Parameters of the BLDRM

Symbol	Parameters	Unit	Value
p_{ro}	Pole pair number of the outer rotor	-	11
p_{ri}	Pole pair number of the inner rotor	-	31
p_{mw}	Pole pair number of modulation winding	-	2
n_o	Outer rotor rated speed	Rpm	200
n_i	Inner rotor rated speed	Rpm	300
T_o	Outer rotor rated torque	N·m	25.22
T_i	Inner rotor rated torque	N·m	23.69
ψ_{fr}	Flux linkage by PMs of the outer rotor	Wb	0.095
ψ_{fm}	Flux linkage by the modulated field	Wb	0.0378

The overall turnaround times, i.e., computation times monitored for both the VMI-based MC-ADRC and VMI-based PI controllers, are shown as follows:

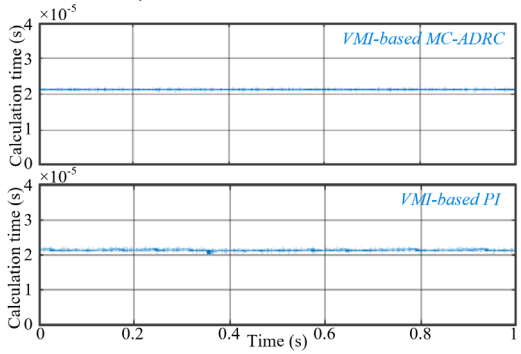

Fig. 13. Turnaround times using the different VMI frame-based controllers.

As shown, the average turnaround times for both methods are approximately 21–22 μs, which accounts for only 21–22% of the total sampling period, indicating a relatively low computational burden. Both controllers can complete all required computations within a single sampling period. Since the only difference between the two methods lies in the speed control loop, the computational times for the respective controllers are also similar.

A. Single Winding Drive

To further demonstrate the presence of torque coupling between the inner and outer rotors, the scenario where only one winding is activated is illustrated in Fig. 14.

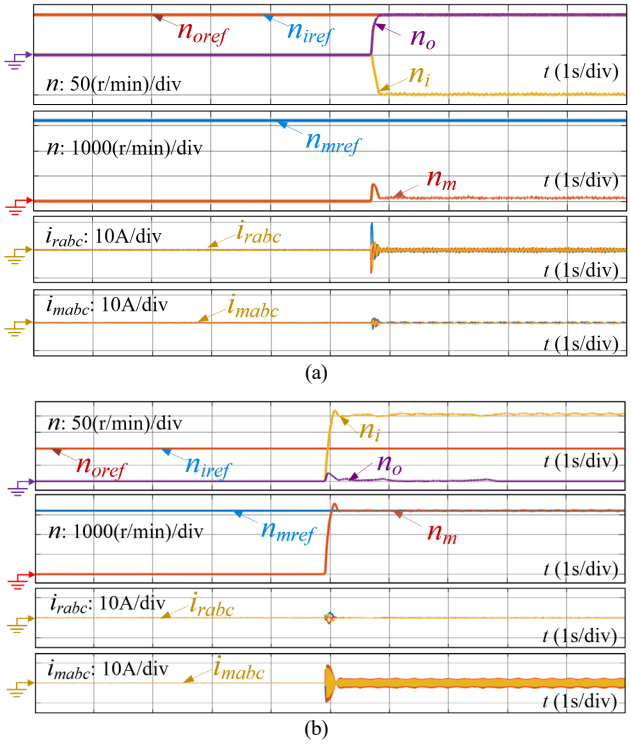

Fig. 14. Response of speed and current when driving with a single winding. (a) Only regular winding works; (b) Only modulation winding works.

As depicted, when only the regular winding is energized, the speed of the outer rotor, i.e., n_o immediately reaches the reference value, n_{oref}. However, due to the coupling torque

between the inner and outer rotors, the inner rotor is dragged to rotate in the same direction at nearly the same speed as the outer rotor, as indicated by n_i. When only the modulated winding is energized, the corresponding speed of its electrical frequency, i.e., n_m, can immediately reach its set value. At this point, the torque generated by the modulated winding exerts forces of approximately equal magnitude but in the opposite direction on the inner and outer rotors. Nevertheless, due to the differing mechanical equations of the inner and outer rotors, their speeds are uncontrollable, failing to attain their set speeds post-stabilization.

B. Abrupt Speed Reference Variation of Dual Rotors

To validate the independent dual-speed regulation of the BLDRM, a VMI-based PI controller and MC-ADRC are employed in the speed control loops, respectively. Speed variation experiments are conducted under two conditions: both rotors operating under no load, and the outer rotor subjected to a load torque of 10.1 N·m. The experimental results are presented in Figs. 15 and 16.

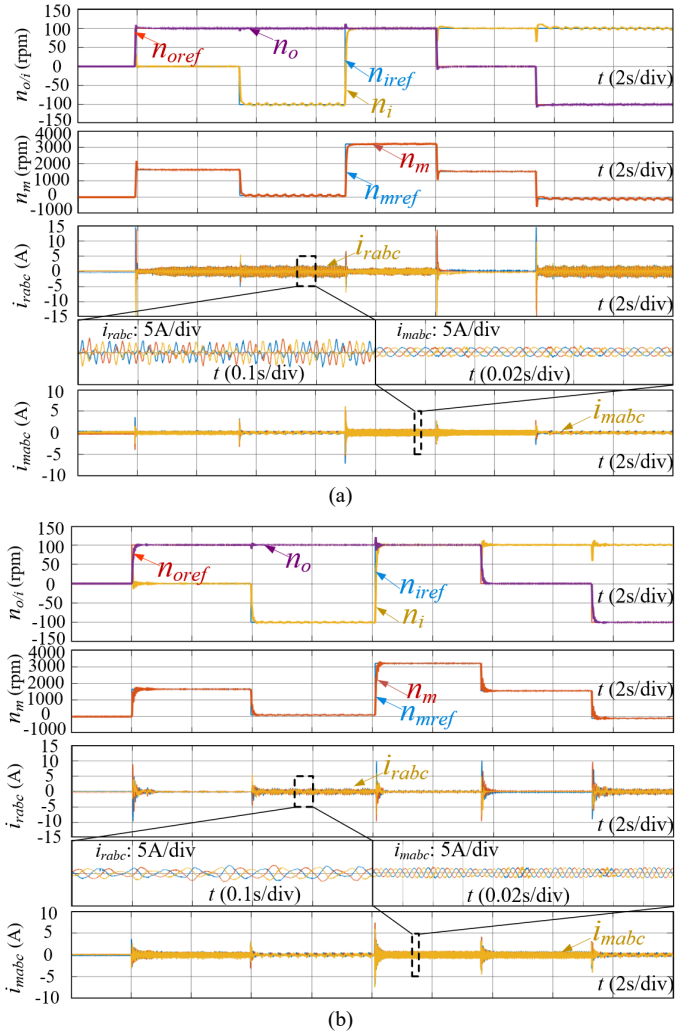

Fig. 15. Experimental results of speed and current under a sudden change of dual rotors' speed with no load. (a) VMI-based PI. (b) VMI-based MC-ADRC.

As shown in Fig. 15, the initial reference speeds are set to zero. In the first stage, the outer rotor accelerates independently. In the second stage, the inner rotor accelerates in the opposite direction; since the positive direction of the inner rotor is defined opposite to that of the outer rotor, both rotors rotate in the same direction at 100 rpm during this phase. In the third stage, the inner rotor reverses its direction, resulting in both rotors rotating in opposite directions at 100 rpm. This represents a typical operating condition for counter-rotating propellers in underwater and aerial vehicles. In the fourth stage, the reference speed of the inner rotor remains unchanged, while the outer rotor decelerates to a stop and then reverses its direction, causing both rotors to rotate in the same direction and at the same speed once again.

It can be observed that both VMI-based PI and MC-ADRC controllers enable the outer rotor to stably track its speed reference throughout the speed variation of the inner rotor, with only small transient fluctuations occurring at the moments of command changes, and vice versa. Similarly, during speed changes of both rotors, the corresponding speed of the modulation winding consistently follows its reference and exhibits a rapid response. These results demonstrate that the introduction of VMI effectively decouples the speed control of the dual rotors, and the proposed methods achieve independent dual-speed regulation.

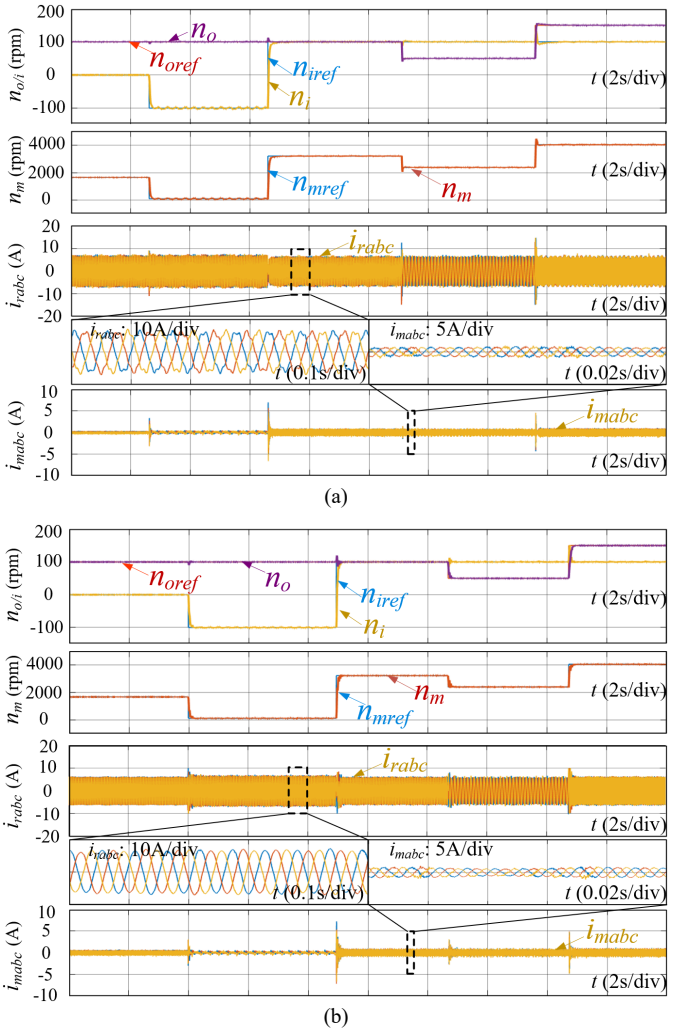

Fig. 16. Experimental results of speed and current under a sudden change of dual rotors' speed with 10.1 N·m load. (a) VMI-based PI. (b) VMI-based MC-ADRC.

Fig. 16 presents the speed variation experiment under a load

torque of 10.1 N·m on the outer rotor. Similar to Fig. 15, both rotors can rapidly and independently track their respective speed references, achieving independent speed regulation. Compared with Fig. 15, under the same dual-rotor speed references, the load applied to the outer rotor primarily affects the regular winding, while the currents in the modulation winding remain largely unaffected. This demonstrates that the BLDRM is capable of decoupling speed and torque.

Specifically, the controller performance under different VMI frameworks is quantitatively compared. The dynamic performance metrics in Fig. 15 are shown in Table II, where the settling time is defined as the time required for the system response to first enter and remain within ±2% of the steady state. The steady-state performance metrics for different VMI-based controllers in Figs. 15 and 16 are shown in Table III.

TABLE II
DYNAMIC PERFORMANCE METRICS FOR DIFFERENT VMI-BASED CONTROLLERS

	n_{oref}=100 rpm, n_{iref} from -100 rpm to 100 rpm		n_{iref} = 0 rpm, n_{oref} from 0 rpm to 100 rpm		
	overshoot n_o	settling time	overshoot n_o	undershoot n_i	settling time
VMI-based PI	12.2%	0.27 s	9.2%	4.2 rpm	0.21 s
VMI-based MC-ADRC	20.6%	0.24 s	3.8%	14.4 rpm	0.27 s

TABLE III
STEADY-STATE PERFORMANCE METRICS FOR DIFFERENT VMI-BASED CONTROLLERS

	No load				*10 N·m load*			
	i_{rabc} (THD)	i_{mabc} (THD)	*Speed fluctuation* n_o	*Speed fluctuation* n_i	i_{rabc} (THD)	i_{mabc} (THD)	*Speed fluctuation* n_o	*Speed fluctuation* n_i
VMI-based PI	102.33%	19.17%	3	5	7.68%	19.95%	4	3
VMI-based MC-ADRC	10.66%	11.05%	3	2.5	3.66%	17.53%	4	2

Table II indicates that, when only the dynamic performance of the speed response is considered, the VMI-based MC-ADRC does not exhibit significant advantages over the VMI-based PI controller. This is mainly because the primary advantage of MC-ADRC over PI lies in its strong disturbance rejection capability, which is particularly evident under sudden load changes or, as in this study, in the presence of intrinsic electromagnetic torque disturbances during steady-state operation, where the speed response is faster and smoother. Notably, the PI controller parameters automatically tuned based on the PMSM within the VMI framework yield favorable dynamic performance, which further validates the effectiveness of the proposed VMI framework. Additionally, the dynamic performance of the MC-ADRC speed controller depends on the accuracy of the model parameters. As derived in Figs. 8 and 11, the estimations of moments of inertia of the dual rotors affect the accuracy of VMI, which may result in suboptimal controller tuning and transient speed oscillations.

It can be seen in Table III that, under no-load conditions, the VMI-based PI control exhibits a THD of 102.33% for regular winding currents and 19.17% for modulated winding. In contrast, the proposed VMI-based MC-ADRC significantly reduces harmonic distortion, achieving a THD of 10.66% for regular winding and 11.05% for modulated winding. This represents a reduction of 91.67% and 8.12%, respectively, compared to the PI-based approach, demonstrating superior harmonic suppression capabilities. When subjected to a 10 N·m load, the VMI-based PI control yields a THD of 7.68% for regular winding and 19.95% for modulated winding. The VMI-based MC-ADRC further improves performance, achieving a THD of 3.66% for regular winding and 17.53% for modulated winding. This corresponds to a reduction of 4.02% in regular winding THD and 2.42% in modulated winding THD.

These results highlight the effectiveness of the proposed VMI-based MC-ADRC approach in significantly reducing current harmonic distortion under both no-load and loaded conditions, outperforming the VMI-based PI control strategy.

C. Abrupt Change in Load Torque of Dual Rotors

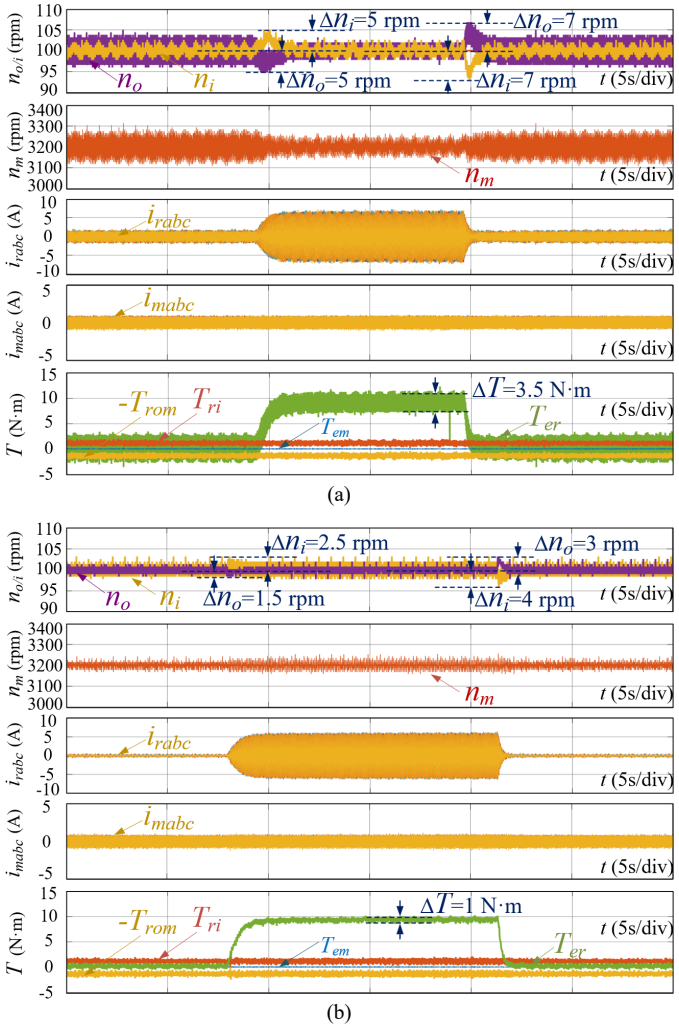

Fig. 17. Experimental results of speed, current, and corresponding calculated torque under a sudden change of 10.1 N·m load torque on the outer rotor. (a) VMI-based PI. (b) VMI-based MC-ADRC.

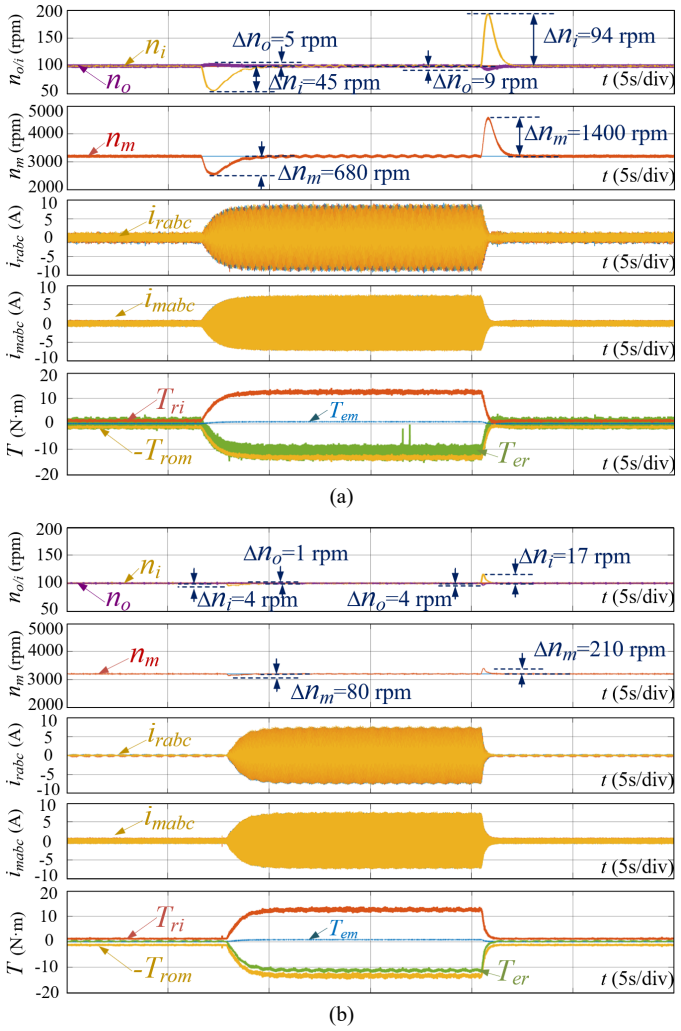

Fig. 18. Experimental results of speed, current, and corresponding calculated torque under a sudden change of 10.1 N·m load torque on the inner rotor. (a) VMI-based PI. (b) VMI-based MC-ADRC.

To evaluate the disturbance rejection capability of the BLDRM dual-speed drive system, a step load torque of approximately 10.1 N·m is applied to the dual rotors, respectively, with the dual rotors counter-rotating at 100 rpm. The rotor speeds, winding currents, and the calculated electromagnetic torques are shown in Fig. 17 and Fig. 18.

As illustrated, when a sudden load torque is applied to the outer rotor, the speed drop of the outer rotor of the VMI-based MC-ADRC is reduced from 5 rpm to 1.5 rpm compared to the VMI-based PI speed controller, and the speed fluctuation of the inner rotor decreases from 5 rpm to 2.5 rpm. When the load torque is suddenly removed, the speed fluctuation of the outer rotor decreases from 7 rpm to 3 rpm, and the speed drop of the inner rotor decreases from 7 rpm to 4 rpm; When a sudden load torque is applied to the inner rotor, the speed drop of the inner rotor of MC-ADRC is reduced from 45 rpm to 4 rpm compared to the VMI-based PI speed controller, representing a 91% reduction. The speed fluctuation of the outer rotor decreases from 5 rpm to 1 rpm. When the load torque is suddenly removed, the speed fluctuation of the inner rotor decreases from 94 rpm to 17 rpm, representing an 82% reduction, and the speed drop of the outer rotor decreases from 9 rpm to 4 rpm. These results indicate that the VMI-based MC-ADRC can significantly mitigate the impact of sudden torque disturbances on both rotors, offering superior disturbance rejection capability.

Furthermore, with the MC-ADRC, the steady-state speed fluctuations are smaller, and the calculated electromagnetic torque ripple from the regular winding is reduced from 3.5 N·m to 1 N·m, a reduction of 71%. The relationship between the electromagnetic torques generated by the regular and modulation windings under separate loading of the dual rotors further validates the accuracy of the analysis.

D. Robustness Experiment

To verify the motor model parameter robustness of the proposed MC-ADRC based BLDRM drive system, the model parameters are altered to 0.8 and 1.5 times their nominal values during steady-state operation with the dual rotors counter-rotating at 100 rpm. The speed and current responses are shown in Fig. 19.

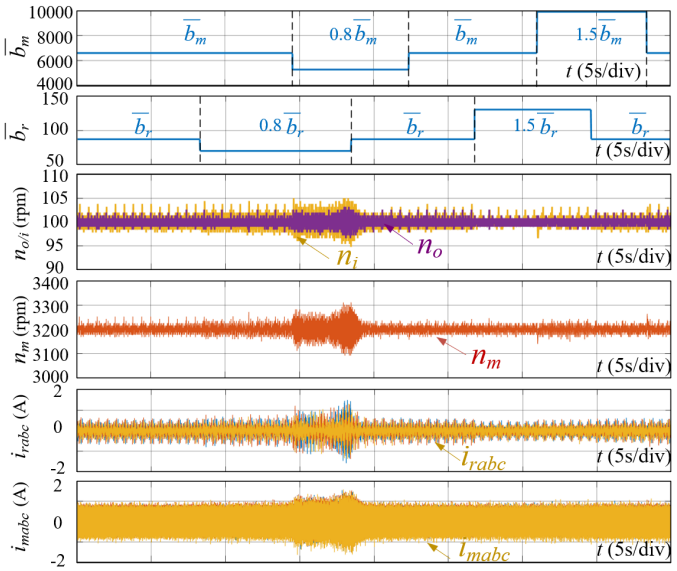

Fig. 19. Experimental results of speed and current under different model parameters of VMI-based MC-ADRC.

It can be observed that when the model parameters are set to 0.8 times their nominal values, both speed and current fluctuations become more pronounced, but stable operation is still maintained. When the parameters are set to 1.5 times their nominal values, there are no significant changes in speed or current, and the system remains stable. This is consistent with the theoretical analysis in Fig. 11. Although model parameters should be selected as accurately as possible, the system can still operate when the parameters are not perfectly accurate.

Notably, even when the system remains stable, significant deviations between the model parameters and their actual values can lead to unacceptable steady-state fluctuations due to noise or degraded dynamic response. In this study, the actual rotational inertia is estimated, which may compromise the robustness of the proposed method and result in a narrow acceptable range for parameter mismatches. Future research will focus on online parameter estimation for the BLDRM, aiming to adaptively optimize the controller and enable broader industrial applications.

VI. Conclusion

In this paper, a novel VMI approach based on the

electromechanical equations of the BLDRM is first proposed, enabling the BLDRM to be equivalently represented as two single-inertia machines. Building upon this model, a detailed control strategy employing MC-ADRC in the speed loops is developed to further torque decoupling and achieve independent control of the dual rotors. Furthermore, comprehensive performance analyses and tuning criteria are provided to ensure the applicability of the proposed method to various types of BLDRMs. Experimental results demonstrate that the VMI-based PI controller and the VMI-based MC-ADRC exhibit similar dynamic performance, which validates the effectiveness of the VMI framework in parameter tuning. Compared to the PI controller, the MC-ADRC shows significantly stronger disturbance suppression capability. Specifically, during counter-rotation, the speed fluctuations of the inner rotor in steady-state are reduced from 5 rpm and 3 rpm to 2.5 rpm and 2 rpm, respectively. The current THD under no-load decreases by 91.67% and 8.12%, and under load by 4.02% and 2.42%. Torque ripple reduces by 71%. Additionally, speed fluctuations during sudden load changes are substantially decreased, with a 91% reduction in the inner rotor during loading, highlighting the effectiveness and superiority of the proposed control scheme.

REFERENCES

[1] K. T. Chau, C. C. Chan, and C. Liu, "Overview of permanent-magnet brushless drives for electric and hybrid electric vehicles," *IEEE Trans. Ind. Electron.*, vol. 55, no. 6, pp. 2246-2257, Jun. 2008.

[2] S. Eriksson and C. Sadarangani, "A four-quadrant HEV drive system," in *Proc. IEEE 56th Veh. Technol. Conf.*, Sep. 2002, pp. 1510-1514.

[3] L. Xu, "Dual-mechanical-port electric machines-concept and application of a new electric," *IEEE Ind. Appl. Mag.*, vol. 15, no. 4, pp. 44-51, Jul./Aug. 2009.

[4] L. Mo, L. Quan, X. Zhu, Y. Chen, H. Qiu, and K.T. Chau, "Comparison and analysis of flux-switching permanent-magnet double-rotor machine with 4QT used for HEV," *IEEE Trans. Mag.*, vol. 50, no. 11, pp. 1-4, Nov. 2014.

[5] J. Druant, H. Vansompel, F. De Belie, J. Melkebeek, and P. Sergeant, "Torque analysis on a double rotor electrical variable transmission with hybrid excitation," *IEEE Trans. Ind. Electron.*, vol. 64, no. 1, pp. 60-68, Jan. 2017.

[6] Y. Wang, S. Niu, and W. Fu, "Sensitivity analysis and optimal design of a dual mechanical port bidirectional flux-modulated machine," *IEEE Trans. Ind. Electron.*, vol. 65, no. 1, pp. 211-220, Jan. 2018.

[7] M. Cheng, P. Han, and W. Hua, "General airgap field modulation theory for electrical machines," *IEEE Trans. Ind. Electron.*, vol. 64, no. 8, pp. 6063-6074, Aug. 2017.

[8] S. Niu, S. L. Ho, and W. N. Fu, "A novel double-stator double-rotor brushless electrical continuously variable transmission system," *IEEE Trans. Mag.*, vol. 49, no. 7, pp. 3909-3912, Jul. 2013.

[9] X. Ren, D. Li, R. Qu, W. Kong, X. Han, and T. Pei, "Analysis of spoke-type brushless dual-electrical-port dual-mechanical-port machine with decoupled windings," *IEEE Trans. Ind. Electron*., vol. 66, no. 8, pp. 6128-6140, Aug. 2019.

[10] L. Cao, Y. Zhou, G. Yang, Y. He, S. Xie, and C. H. T. Lee, "Decoupling analysis of brushless dual-mechanical-port dual-electrical-port machines," *IEEE Trans. Ind. Electron.*, vol. 71, no. 5, pp. 4361-4374, May 2024.

[11] M. Bouheraoua, J. Wang, and K. Atallah, "Design and implementation of an observer-based state feedback controller for a pseudo direct drive," *IET Electr. Power Appl*., vol. 7, no. 8, pp. 643-653, Oct. 2013.

[12] X. Han et al., "Modeling and drive control of a brushless dual-mechanical-port machine with integrated winding," *IEEE Trans. Ind. Electron*., vol. 68, no. 3, pp. 2059-2071, Mar. 2021.

[13] M. Jiang and S. Niu, "A high-order harmonic compound rotor based brushless dual-electrical-port dual-mechanical-port machine," *IEEE Trans. Ind. Electron.*, vol. 71, no. 6, pp. 5463-5473, Jun. 2024.

[14] H. Zhao, C. Liu, Z. Song, and S. Liu, "Design and control of a new compound double-rotor electric machine for hybrid propulsion system," *IEEE Trans. Power Electron.*, vol. 37, no. 3, pp. 3283-3296, Mar. 2022.

[15] X. Han et al., "Flexible energy conversion control strategy for brushless dual-mechanical-port dual-electrical-port machine in hybrid vehicles," *IEEE Trans. Power Electron.*, vol. 34, no. 4, pp. 3910-3920, Apr. 2019.

[16] L. Xu, Y. Zhang, and X. Wen, "Multioperational modes and control strategies of dual-mechanical-port machine for hybrid electrical vehicles," *IEEE Trans. Ind. Appl.,* vol. 45, no. 2, pp. 747-755, Mar.-Apr. 2009.

[17] X. Luo, and S. Niu, "A novel contra-rotating power split transmission system for wind power generation and its dual MPPT control strategy," *IEEE Trans. Power Electron.*, vol. 32, no. 9, pp. 6924-6935, Sept. 2017.

[18] H. Chen et al., "A permanent magnet brushless doubly fed electric machine for variable-speed constant-frequency wind turbines," *IEEE Trans. Ind. Electron.*, vol. 70, no. 7, pp. 6663-6674, Jul. 2023.

[19] M. Jiang, S. Niu, and C. Chuen Chan, "A high-order-harmonic compound-rotor based brushless doubly-fed machine for variable speed constant frequency wind power generation," *IEEE J. Emerg. Sel. Topics Power Electron.*, vol. 13, no. 2, pp. 1492-1502, Apr. 2025.

[20] Z. Ran, Z. Q. Zhu, Y. Zhou, L. Chen, and L. Yang, "A novel counter-rotating single-stator dual-internal-rotor permanent magnet machine," *IEEE Trans. Transp. Electrific*., vol. 11, no. 1, pp. 4992-5004, Feb. 2025.

[21] H. Shin, J. Chang, and D. Hong, "Design and characteristics analysis of coaxial magnetic gear for contra-rotating propeller in yacht," *IEEE Trans. Ind. Electron*., vol. 67, no. 9, pp. 7250–7259, Sep. 2020.

[22] C. Tong, J. Lang, J. Bai, P. Zheng, and D. Ma, "Deadbeat-direct torque and flux control of a brushless axial-flux magnetic-geared double-rotor machine for power-splitting HEVs," *IEEE Trans. Ind. Electron*., vol. 70, no. 9, pp. 8734-8745, Sep. 2023.

[23] X. Liu, W. Kong, R. Qu, and X. Han, "Dynamic performance improvement control of brushless dual-electrical-port dual-mechanical-port machine with integrated winding," in *Proc. ICEM*, Gothenburg, Sweden, 2020, pp. 2169-2175.

[24] J. Yang, S. Li, and X. Yu, "Sliding-mode control for systems with mismatched uncertainties via a disturbance observer," *IEEE Trans. Ind. Electron*., vol. 60, no. 1, pp. 160-169, Jan. 2013.

[25] X. Zhang, L. Sun, K. Zhao, and L. Sun, "Nonlinear speed control for PMSM system using sliding-mode control and disturbance compensation techniques," *IEEE Trans. Power Electron.*, vol. 28, no. 3, pp. 1358-1365, Mar. 2013.

[26] J. Liu, H. Li, and Y. Deng, "Torque ripple minimization of PMSM based on robust ILC via adaptive sliding mode control," *IEEE Trans. Power Electron.*, vol. 33, no. 4, pp. 3655-3671, Apr. 2018.

[27] X. Tang and S. Niu, "Coherent vector-based model predictive control with zero-sequence component injection for three-level NPC inverter fed PMSM drives," *IEEE Trans. Power Electron.*, vol. 40, no. 10, pp. 14686-14696, Oct. 2025.

[28] Z. Sun, J. Wen, X. Yuan, G. Ma, S. Niu, and K. T. Chau, "A novel robust dead-beat structure for double vector model predictive control in three-level inverter fed PMSM drives," *IEEE Trans. Power Electron.*, doi: 10.1109/TPEL.2025.3575075.

[29] X. Tang, S. Niu, K. T. Chau, X. Yuan, and W. L. Chan, "Model predictive control of three-level NPC inverter-fed PMSM drives based on a novel vector-selection scheme," *IEEE J. Emerg. Sel. Topics Power Electron.*, vol. 13, no. 3, pp. 3284-3296, Jun. 2025.

[30] E. Sariyildiz, R. Oboe, and K. Ohnishi, "Disturbance observer-based robust control and its applications: 35th anniversary overview," *IEEE Trans. Ind. Electron*., vol. 67, no. 3, pp. 2042-2053, Mar. 2020.

[31] J. Han, "From PID to active disturbance rejection control," *IEEE Trans. Ind. Electron.*, vol. 56, no. 3, pp. 900-906, Mar. 2009.

[32] Z. Gao, "Scaling and bandwidth-parameterization based controller tuning," in *Proc. Amer. Control Conf*., 2003, pp. 4989-4996.

[33] J. Yang, W. -H. Chen, S. Li, L. Guo, and Y. Yan, "Disturbance/uncertainty estimation and attenuation techniques in PMSM drives—a survey," *IEEE Trans. Ind. Electron.*, vol. 64, no. 4, pp. 3273-3285, Apr. 2017.

[34] Y. Chen, M. Yang, J. Long, W. Qu, D. Xu, and F. Blaabjerg, "A moderate online servo controller parameter self-tuning method via variable-period inertia identification," *IEEE Trans. Power Electron.*, vol. 34, no. 12, pp. 12165-12180, Dec. 2019.